Available online at www.sciencedirect.com
ScienceDirect
Trans. Nonferrous Met. Soc. China 35(2025) 4021−4037
Transactions of Nonferrous Metals Society of China
www.tnmsc.cn

Significantly improving corrosion resistance of Al−5Zn alloy by adjusting its Zn phase and dislocation distribution

Yu-na WU[1,2], Chong-guang YUE[1,2], Ting YUAN[3],
Lin WANG[1], Dan SONG[1], Huan LIU[1], Jing-hua JIANG[1], Jing BAI[4], Ai-bin MA[1]

1. College of Materials Science and Engineering, Hohai University, Changzhou 213200, China;
2. Suqian Research Institute, Hohai University, Suqian 223800, China;
3. School of Chemistry and Materials Engineering, Changshu Institute of Technology, Changshu 215500, China;
4. School of Materials Science and Engineering, Southeast University, Nanjing 211189, China

Received 12 March 2024; accepted 16 December 2024

Abstract: A balance between strength and corrosion resistance in 7xxx series aluminum (Al) alloys is difficult to achieve because of their diverse secondary phases. In this study, the Al−5Zn binary alloy was selected as a simplified representative of the 7xxx series Al alloys, and four distinct equal-channel angular pressing (ECAP) passes of 4, 8, 12, and 16 were used to adjust the Zn phase and dislocation distribution in the alloy. The corrosion behavior and mechanical properties of the alloy were evaluated by performing electrochemical and tensile tests as well as optical microscopy, scanning electron microscopy, and transmission electron microscopy. The results indicate that the Al−5Zn alloy exhibits the highest polarization resistance value and the lowest corrosion current density after 16 ECAP passes. Additionally, its overall mechanical properties with ultimate tensile strength of 224 MPa, yield strength of 199 MPa, and elongation of 21.3% are excellent. The fragmentation and uniform distribution of the Zn phase as well as the even distribution of dislocations contribute to exceptional corrosion resistance and mechanical properties.

Key words: Al−Zn alloy; corrosion resistance; Zn phase; dislocation; mechanical properties

1 Introduction

The 7xxx series (Al−Zn−Mg−Cu) aluminum (Al) alloys are promising light-metal alloys for offshore applications because of their superior specific strength and corrosion resistance [1]. Their mechanical properties can be improved by adding elements (Zr, Sc, Ag, etc.) to the primary alloy elements (Zn, Mg, and Cu) to generate various reinforcing phases [2−5]. However, in a maritime environment, the reinforcing phases form numerous corrosion cells within the Al matrix, resulting in a severe reduction in corrosion resistance [6,7]. Therefore, it is crucial to overcome the tradeoff between the strength and the corrosion resistance of the 7xxx series Al alloys.

Over the past two decades, equal-channel angular pressing (ECAP) has been widely used to enhance the mechanical properties of 7xxx series Al alloys by altering their microstructure (i.e. refining grains, starting dislocations, and controlling secondary phases) [8−10]. In numerous studies, it has been reported that the strengthening of alloys consistently causes a decrease in their corrosion resistance [11,12]. This is attributed to the following reasons: (1) Fine-grained Al alloys have more susceptible corrosion sites after applying the ECAP

Corresponding author: Yu-na WU, Tel: +86-13585199947, E-mail: wuyuna@hhu.edu.cn;
Huan LIU, Tel: +86-15951082775, E-mail: liuhuanseu@hhu.edu.cn
https://doi.org/10.1016/S1003-6326(25)66927-5

compared with coarse-grained Al alloys [13]. (2) ECAP introduces a large number of tangled dislocations in the alloys, which are the preferential corrosion sites due to stress concentration [14]. (3) The secondary phases (such as $MgZn_2$, $CuMgAl_2$, etc.) precipitate during the ECAP process and form numerous corrosion microcells with the Al matrix [15−17]. However, some alternative theories have been proposed. For example, LI et al [18] developed an ultrafine grain structure of the Al−Zn−Mg−Cu alloy by employing a combined deformation process involving ECAP and post-cold rolling (CR); their results showed that a rolling deformation in the 20%−40% range causes a decrease in the grain size from 0.931 to 0.501 μm and an enhancement in the alloy corrosion resistance. This is attributed to the grain refinement treatment, which increases the area fraction of the grain boundary and expedites the production of the passivation film by increasing its thickness and density; as a result, the corrosion resistance of the deformed alloy is improved [19]. Additionally, it has been reported that ECAP affects the characteristics of secondary phases, thereby improving the corrosion resistance of Al alloys [20]. QUARTIERMEISTER et al [21] reported an enhancement in the AA1015 Al alloy corrosion resistance by increasing the number of ECAP passes to 8; this was attributed to the decrease in the size of the secondary phase. By reducing the pitting sensitivity and inhibiting the overall microgalvanic reaction, the fine secondary phase particles can improve the alloy corrosion resistance [22,23].

In summary, the combined effect of various secondary phases primarily determines the impact of ECAP on the corrosion resistance of Al alloys. However, the impact of individual secondary phases on the corrosion resistance of 7xxx series Al alloys, and the underlying mechanisms, have received little attention. The micron-sized and nano-sized Zn phases exhibit similar behavior to the micron-sized $MgZn_2$ and nano-sized η phases, respectively, serving as initial corrosion sites in Al alloys [24]. In this study, we employed the Al−5Zn binary alloy as a simple approximation of the Al−Zn−Mg alloys. We applied four distinct ECAP passes (4, 8, 12, and 16 passes) to control the Zn phase and dislocations. By examining the size and distribution effects of the Zn phase on the corrosion behavior of the Al−5Zn alloy and their mechanisms, a deep understanding of the impact of the $MgZn_2$ phase on the corrosion resistance of 7xxx series alloys was obtained. By controlling the morphology of the secondary phases and the distribution of dislocations, an optimal combination of mechanical properties and corrosion resistance was also achieved.

2 Experimental

2.1 Sample preparation

Industrial pure Al and Al−65wt.%Zn alloy were the raw materials for preparing Al−5Zn alloy, while C_2Cl_6 was the refined agent. The targeted alloy was smelted in a vacuum static furnace [25], which was used to evacuate the melting for 30 min to degas after all the smelting processes (including adding intermediate alloys, refining, etc.) were completed. The actual chemical composition of the alloy is shown in Table 1. The Al−5Zn alloy ingot was marked as “as-cast”. The as-cast Al−5Zn alloy was dissolved at 470 °C for 4 h, marked as “as-ss”. The as-ss Al−5Zn alloy cut into 45 mm × 19.5 mm × 19.5 mm experienced different passes of ECAP (4, 8, 12, and 16 passes) at room temperature. The ECAP extrusion process is depicted in Fig. 1.

Table 1 Actual composition of Al−5Zn alloy (wt.%)

Zn	Cu	Fe	Si	Al
5.58	0.01	0.145	0.07	Bal.

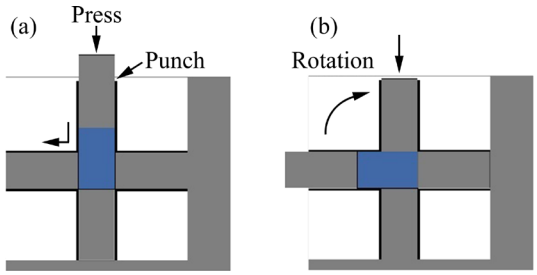

Fig. 1 Schematic diagrams of ECAP extrusion process: (a) Single pass ECAP; (b) Rotation sample

2.2 Microstructure characterization

The microstructures were characterized by an optical microscope (OM, Olympus BX51 M), a Hitachi S3400 N scanning electron microscope (SEM) equipped with an energy dispersive spectroscope (EDS) and an electron back-scattered diffraction

(EBSD)), and an FEI Tecnai G2 T20 transmission electron microscope (TEM).

The samples for OM and SEM observation were prepared by the following process: The alloy sheets under different conditions were ground using SiC sandpapers with grit ranging from 180# to 2000#, cleaned in alcohol, polished using a 3.5 μm diamond, and then dried in cold air. The metallographic erosion solution was 1.5 vol.% HCl + 2.5 vol.% HNO_3 + 1 vol.% HF + 95 vol.% H_2O. About 30 s passed during the erosion process. Prior to the EBSD test, the samples were electrolytically polished in 10 vol.% $HClO_4$ solution at 0 °C for 120 s with a voltage of 25 V and a current of 0.4−0.5 A. The EBSD data were analyzed and processed by Channel 5 software.

The samples used in TEM observation were ground with SiC sandpapers to a thickness of about 70 μm. They were then ion-thinned using the Gatan PIPS II 695 instrument after being stamped into discs with a diameter of 3 mm.

2.3 Corrosion resistance and mechanical properties tests

The electrochemical performance tests were carried out at the CHE660 electrochemical work-station using a conventional three-electrode system in a 3.5 wt.% NaCl solution. The working electrode (with a working area of 1 cm^2) was the sample to be evaluated, the reference electrode was a saturated calomel electrode (SCE), and the counter electrode was a platinum electrode. Each sample was tested for open circuit potential (OCP), alternating current impedance, and dynamic polarization potential. The OCP scanning time was 1 h, the frequency range of the electrochemical impedance spectroscopy (EIS) was 10 mHz−10 kHz, and the perturbation amplitude was 10 mV. The potentiodynamic polarization (PDP) curves were measured from a position 0.25 V lower than the OCP to the positive direction at a scanning rate of 0.5 mV/s. The scanning was terminated when the breakdown voltage reached from −2 to −3 V. The surface corrosion morphology was examined using an OM.

The corrosion immersion experiment was carried out in a 3.5 wt.% NaCl solution at 25 °C for 7 d. Following the immersion, the depth of the corrosion pits on the samples was examined using an OM.

Tensile tests were conducted on the samples at room temperature using a Suns-UTM4294X machine at a speed of 0.5 mm/min. The dimensions of the dog-bone specimens were 6 mm × 2 mm × 2 mm [26].

3 Results

3.1 Surface morphologies of ECAPed Al−5Zn alloys

The microstructures of the as-cast and as-ss Al−5Zn samples observed using OM and SEM are shown in Fig. 2. The as-cast sample shown in Figs. 2(a, b) consists of an equiaxed Al matrix and coarse secondary phases, which extend along the grain edges. Figures 2(c, d) show that the grain boundaries of the as-ss sample become fuzzy compared with those of the as-cast sample, and the solid solution leads to fine secondary phases. The EDS analysis indicates that the secondary phases correspond to the Zn phases (Figs. 2(e, f)).

Figure 3 shows OM and SEM micrographs of the samples after different ECAP passes. Figures 3(a, b) show that after 4 passes, the grains are elongated, and the Zn phases are fragmented along the extrusion direction (ED). Figures 3(c, d) show that after 8 passes, the width of the elongated grains decreases, and there are less obvious changes in the Zn phases. Compared with that of 4 passes (~6 μm) and 8 passes (~4 μm), the length of the Zn phase is reduced to 2 μm, and its size is drastically reduced after 12 and 16 passes. Additionally, Figs. 3(f, h) show a more uniform distribution of the Zn phases. Therefore, by increasing the number of ECAP passes, the Zn phase is finely fragmented and uniformly distributed along the shearing direction. Furthermore, the shape of the secondary phase progressively shifts from a rod to a sphere.

Figures 4 and 5 show the EBSD analysis results of the Al−5Zn alloy, which was processed over a range of ECAP passes. The ECAPed samples are dominated by strip grains, which change in width as the number of passes increases. The strip grains are relatively wide after 4 passes. In contrast, their width decreases after 8 and 12 passes. However, with further deformation to 16 passes, the grain width increases again. After 4 passes, the average grain size is 3.3 μm (Fig. 5(a)). The subgrain boundaries inside the strip grains grow into new grain boundaries due to ECAP,

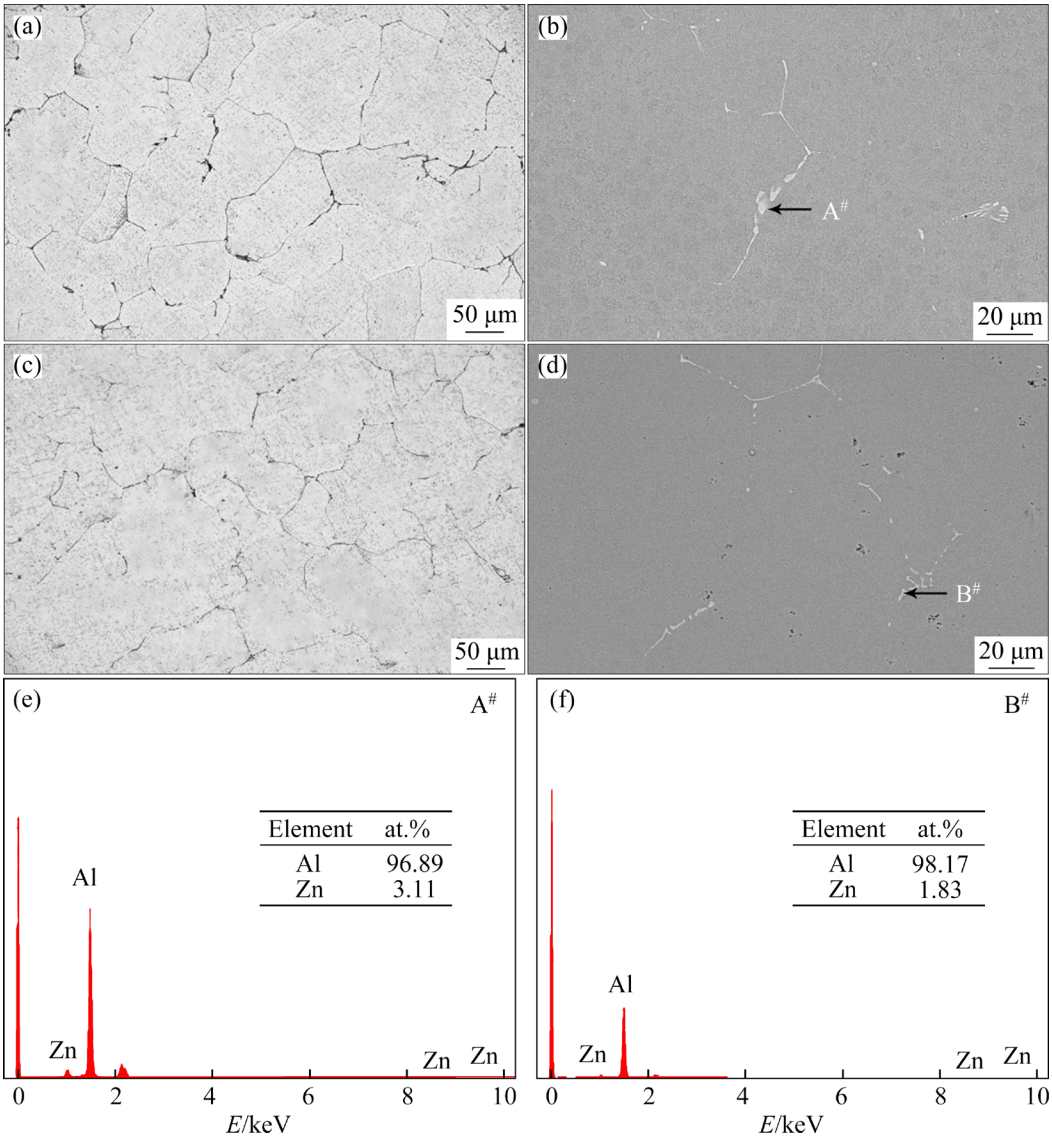

Fig. 2 Surface morphologies of Al−5Zn alloys observed by OM (a, c) and SEM (b, d) and their EDS data (e, c): (a, b, e) As-cast; (c, d, f) As-ss

resulting in the appearance of a few additional equiaxed grains (Fig. 4(a)). After 8 passes, the average grain size is reduced to 2.0 μm (Fig. 5(b)). Figure 4(b) shows a further refinement of the coarse grains. In addition, strip-like coarse grains exhibiting numerous subgrain boundaries are also present. When the deformation increases to 12 passes, the deformed grains are further elongated and refined to form an obvious layered structure (Fig. 4(c)). The grain size after 12 passes remains the same as that after 8 passes because small grains combine and generate large grains. Because of the significant accumulated strain, after 16 passes, nearly all grains increase in size (with an average grain size of 2.6 μm, Fig. 5(d)). Moreover, subgrains with the large misorientation (as shown by the black arrow in Fig. 4(d)) and many new grains (as shown by the blue arrow in Fig. 4(d)) appear inside the large grains.

Figure 6 shows statistical recrystallization maps of the Al−5Zn alloys after various ECAP passes. After 4 passes, the sample exhibits a 13% recrystallization rate (Fig. 6(a)), and all grains are equiaxed in shape (Fig. 4(a)). As the number of passes increases, the recrystallization rate decreases, reaching a minimum of 8% after 12 passes (Fig. 6(c)). In addition, the recrystallized grain size decreases, and a few recrystallized grains appear in the strips (Figs. 4(b) and (c)). However, after 16 passes, the recrystallization rate increases significantly to 22%, as shown in Fig. 6(d).

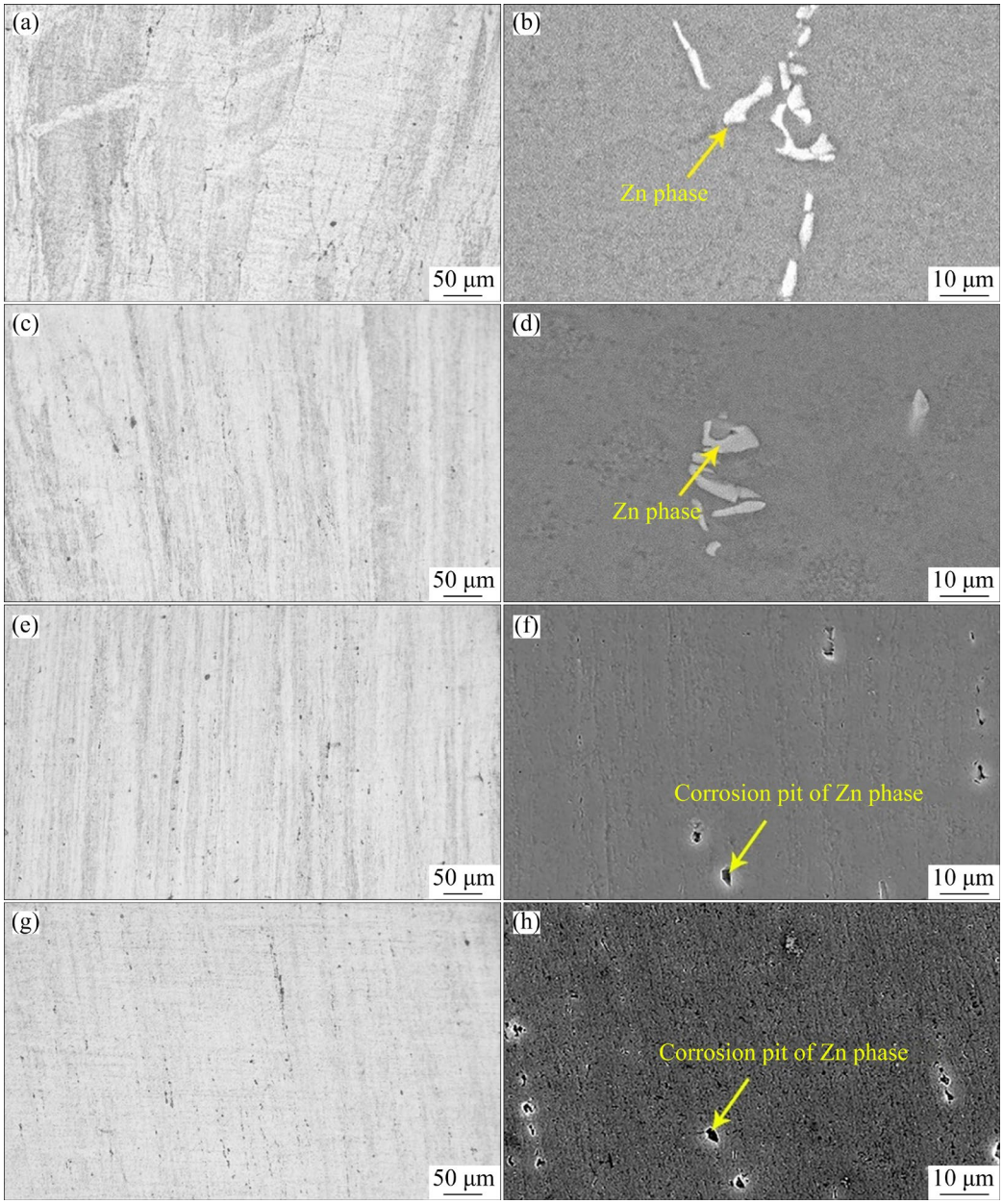

Fig. 3 Surface morphologies of ECAPed Al−5Zn alloys by OM (a, c, e, g) and SEM (b, d, f, h): (a, b) 4 passes; (c, d) 8 passes; (e, f) 12 passes; (g, h) 16 passes

The kernel average misorientation (KAM) in the Al−5Zn alloys after different ECAP passes is presented in Fig. 7. After 4 passes, many dislocation tangles in the sample are observed. However, the aggregated dislocations eventually disperse as the number of passes increases. After 16 passes, the dislocations are evenly distributed across the sample.

Figure 8 shows that the average of all KAM angle values of the ECAPed samples is ~0.57. The average dislocation density of the samples is almost the same; however, a serious local entanglement and an uneven dislocation distribution in the samples are observed after 4, 8, and 12 passes.

Figure 9 shows typical TEM microstructures of the Al−5Zn alloys after different ECAP passes. The diffraction pattern of the selected area shows that the black precipitates are elliptical and irregularly shaped polygons along the grain boundaries. These nano-sized Zn phases are caused by the dynamic precipitation during ECAP. The length of the Zn phases ranges from 41 to 146 nm after 4 passes. After 8 ECAP passes, the length of the Zn phases slightly decreases; the maximum length is ~132 nm, while the minimum length is ~29 nm. After 12 passes, the average length of the Zn phases decreases obviously;

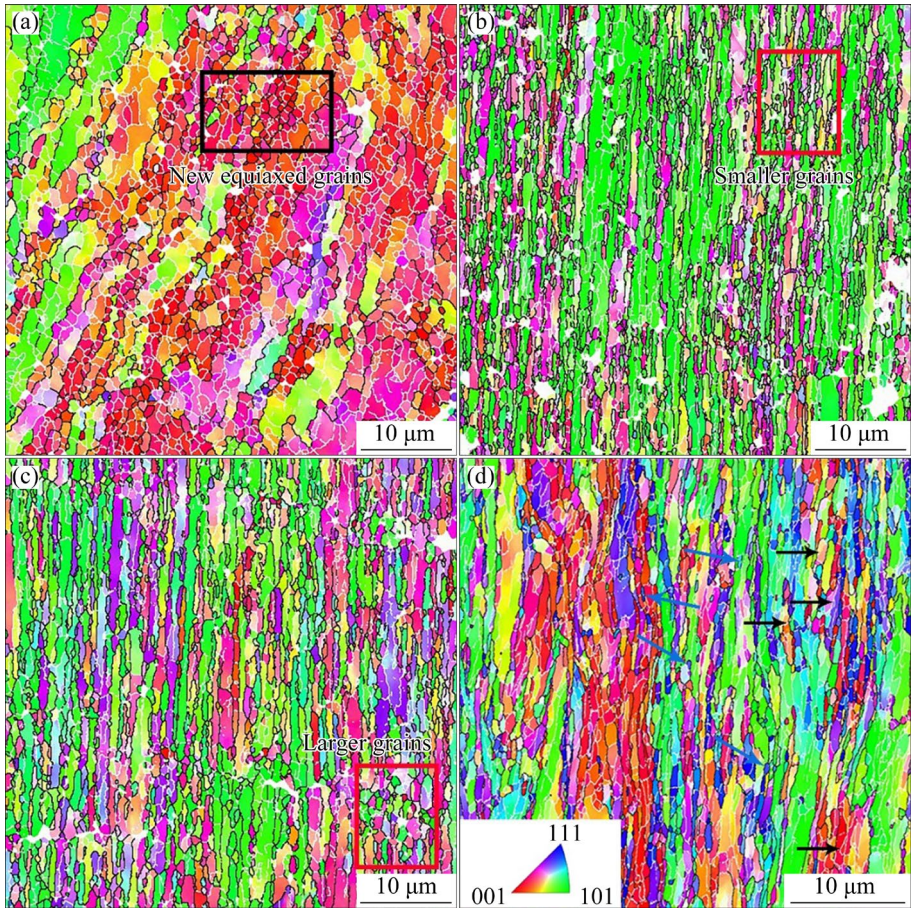

Fig. 4 OM images of ECAPed Al−5Zn alloys observed by EBSD: (a) 4 passes; (b) 8 passes; (c) 12 passes; (d) 16 passes (The black line represents large angle grain boundary and white line represents small angle grain boundary)

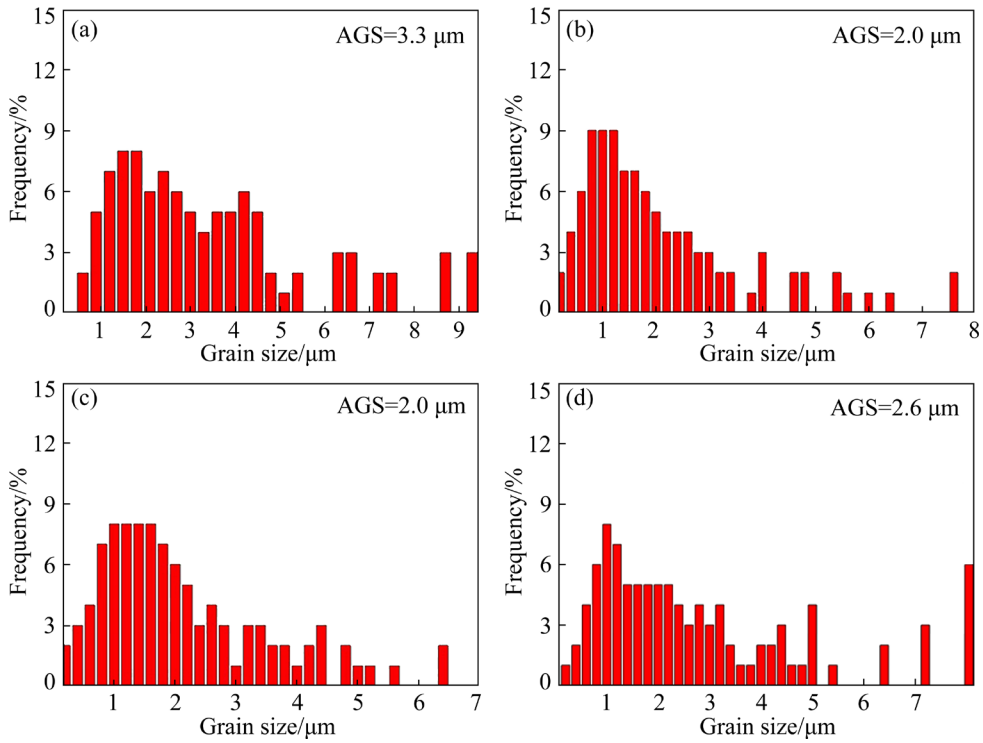

Fig. 5 Average grain size (AGS) of Al−5Zn alloys after different ECAP passes: (a) 4 passes; (b) 8 passes; (c) 12 passes; (d) 16 passes

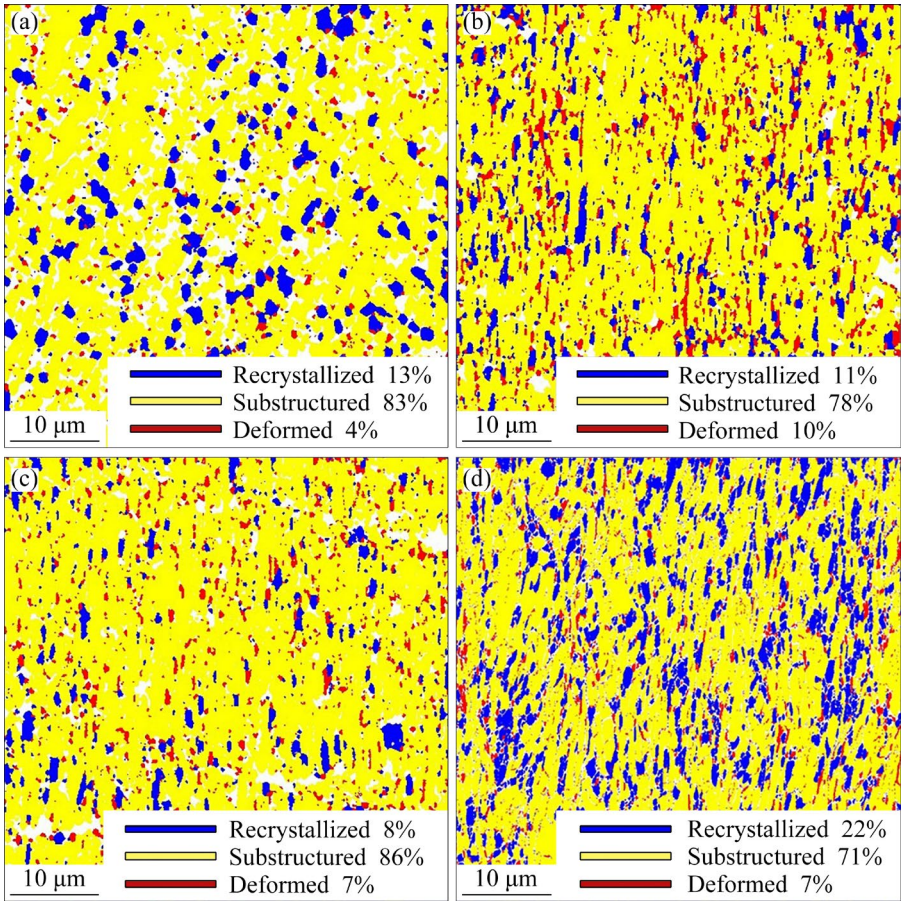

Fig. 6 Statistical recrystallization maps of Al−5Zn alloys after different ECAP passes: (a) 4 passes; (b) 8 passes; (c) 12 passes; (d) 16 passes

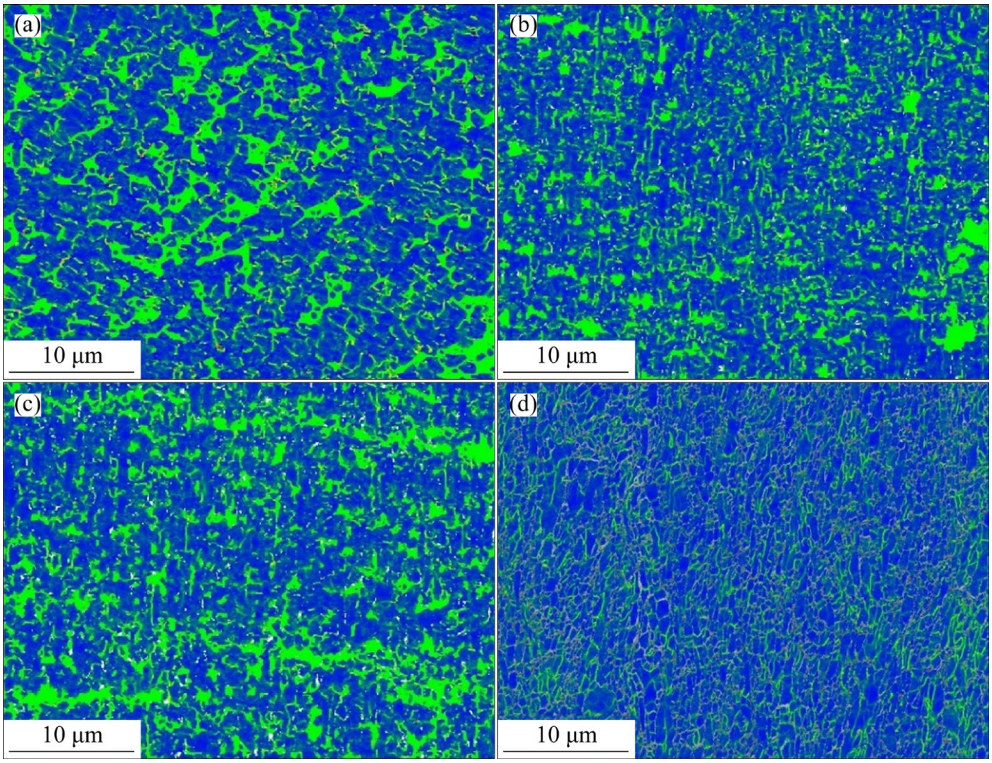

Fig. 7 EBSD maps of Al−5Zn alloys after different ECAP passes: (a) 4 passes; (b) 8 passes; (c) 12 passes; (d) 16 passes

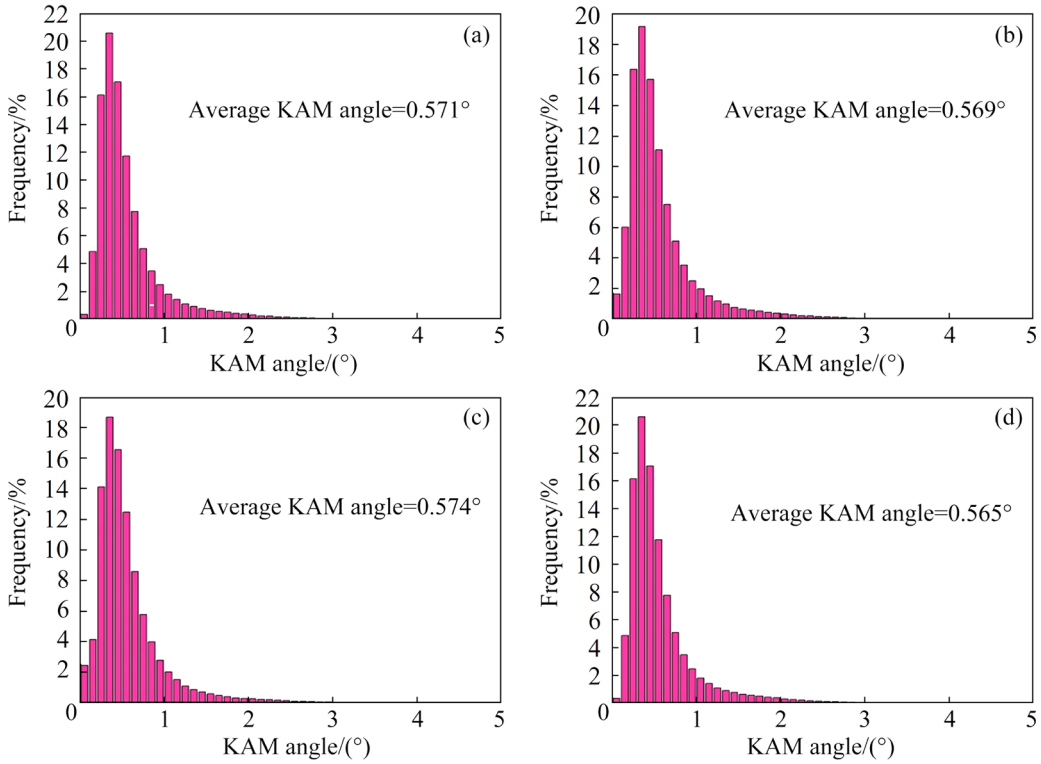

Fig. 8 KAM angles of Al−5Zn alloys after different ECAP passes: (a) 4 passes; (b) 8 passes; (c) 12 passes; (d) 16 passes

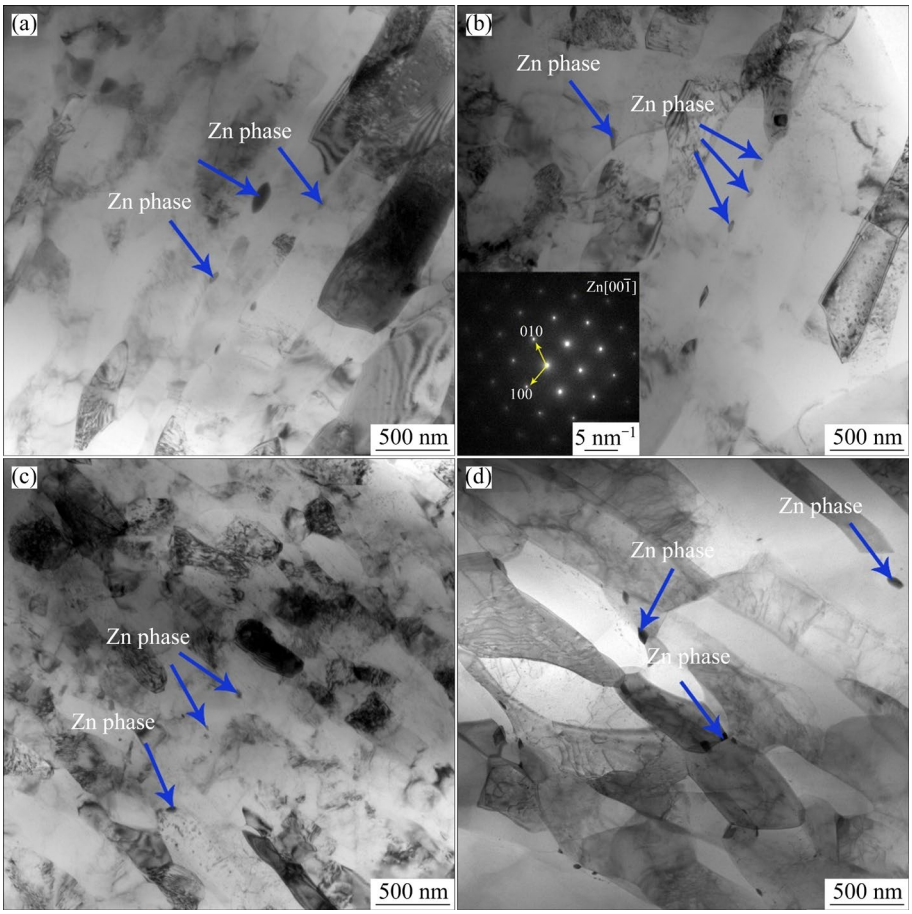

Fig. 9 Bright-field TEM images exhibiting precipitates along grain boundaries of Al−5Zn alloys after different ECAP passes: (a) 4 passes; (b) 8 passes; (c) 12 passes; (d) 16 passes

moreover, the length distribution of these phases becomes more homogeneous with a maximum length of ~76 nm and a minimum length of ~15 nm. After 16 passes, the length of the Zn phases increases again, reaching a maximum of 123 nm and a minimum of 33 nm.

Typical TEM images showing the dislocations and subgrains in the Al−5Zn alloys after different ECAP passes are presented in Fig. 10. The blue arrows in Fig. 10(a) indicate that after 4 passes, the high-density dislocation tangles are ubiquitous. After 8 passes, although dislocation tangles exist, the dislocation density in many cell structures decreases, as indicated by the yellow arrows in Fig. 10(b). After 12 passes, the dislocation tangles nearly vanish, revealing numerous subgrains, as indicated by the red arrows in Fig. 10(c). After 16 passes, the dislocations become evenly distributed, resembling the neatly arranged dislocations shown in Fig. 10(d).

3.2 Tensile properties

Figure 11 shows the engineering stress–strain curves of the Al−5Zn alloys after different ECAP passes. The ultimate tensile strength (UTS) of the as-cast sample is 97 MPa, and the yield strength (YS) is 43 MPa. After 4 passes, the elongation (EL) becomes 17.5%, and the UTS and YS increase to 167 and 162 MPa, respectively. As the number of extrusion passes increases, the strength and ductility increase simultaneously. After 12 passes, the UTS, YS, and EL of the ECAPed sample reach 238 MPa, 214 MPa, and 20.8%, respectively. After 16 passes, UTS and YS decrease to 224 and 199 MPa, respectively, and EL increases to 21.3%. The detailed tensile properties are presented in Table 2.

3.3 Corrosion resistance

Figure 12 shows representative EIS data of different samples in a 3.5 wt.% NaCl solution. Figure 12(a) shows that the Nyquist plots of the samples after different ECAP passes exhibit the same evolution trend. All curves include a capacitive loop and two inductive loops, indicating that ECAP does not change the corrosion mechanism of the Al−5Zn alloy. However, the radius of the capacitive loop varies, indicating different polarization resistances (R_p).

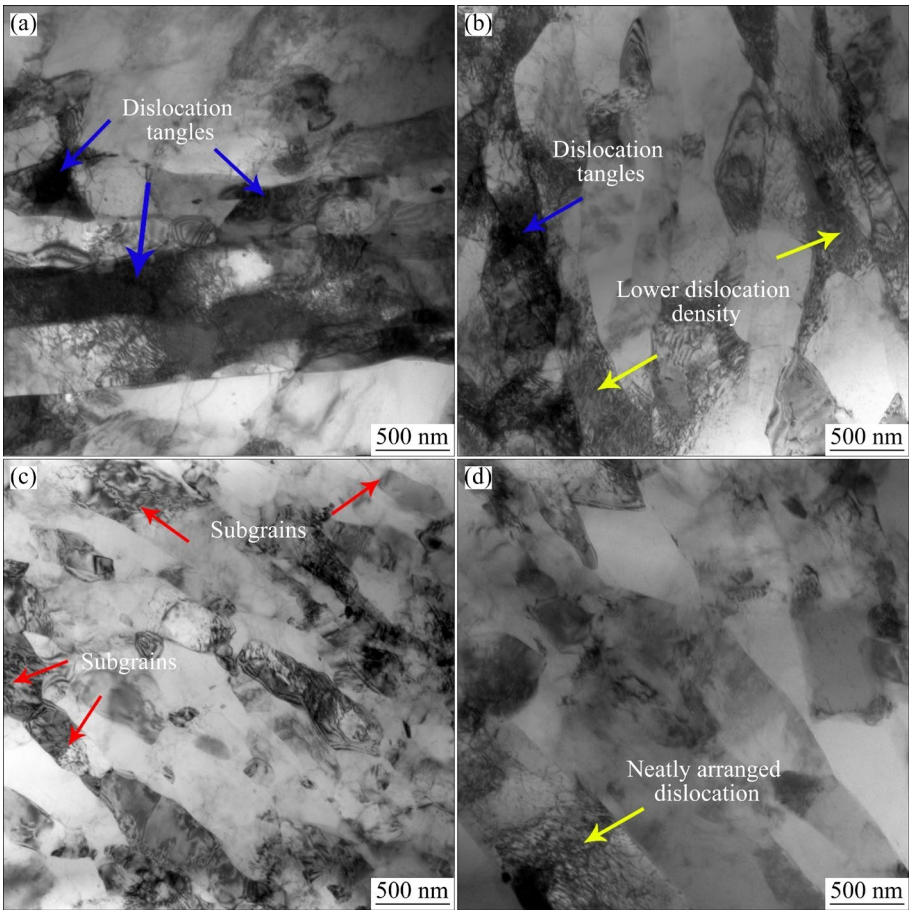

Fig. 10 Typical TEM images revealing dislocations and sub-grains of Al−5Zn alloys after different ECAP passes: (a) 4 passes; (b) 8 passes; (c) 12 passes; (d) 16 passes

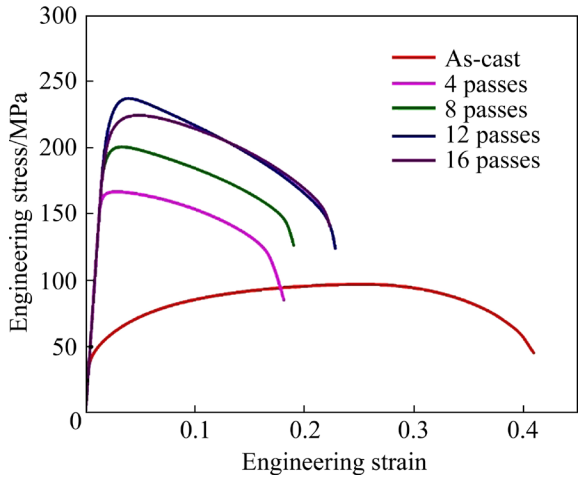

Fig. 11 Typical engineering stress−strain curves of as-cast and ECAPed Al−5Zn alloys

Table 2 Tensile properties of Al−5Zn alloys after different ECAP passes

Sample	UTS/MPa	YS/MPa	EL/%
As-cast	97	43	40.6
4 passes	167	162	17.5
8 passes	200	186	18.1
12 passes	238	214	20.8
16 passes	224	199	21.3

Among them, the as-cast sample has the smallest radius of the capacitive loop and R_p value (3038 Ω·cm^2). After 4 and 8 passes, the radii of the capacitive loops and the R_p values (5527 and 5251 Ω·cm^2, respectively) are very close but higher than those of the as-cast sample. After 12 and 16 passes, the radii and R_p exhibit their highest values (R_p becomes 7841 and 9706 Ω·cm^2, respectively). The impedance moduli in the Bode plots are similar, as shown in Fig. 12(b). The as-cast sample exhibits the lowest impedance modulus in the low-frequency region. The modulus increases after ECAP, with the samples processed for 4 and 8 passes showing intermediate values, and those processed for 12 and 16 passes achieving the highest values. This trend indicates that the low-frequency impedance modulus of the Al−5Zn alloy generally increases with increasing the number of ECAP passes.

Figure 13 shows a circuit equivalent to the EIS of the Al−5Zn alloy, where R_s is the solution resistance, CPE_1 is the constant phase angle element of the double-layer capacitor, and L_1, R_1 and L_2, R_2 correspond to the inductances and reaction resistances of Al^{3+} and Zn^{2+}, respectively. According to the fitting results shown in Table 3, R_s value is stable at ~10 Ω·cm^2, indicating that the solution environment for each sample is similar and the experimental results are comparable.

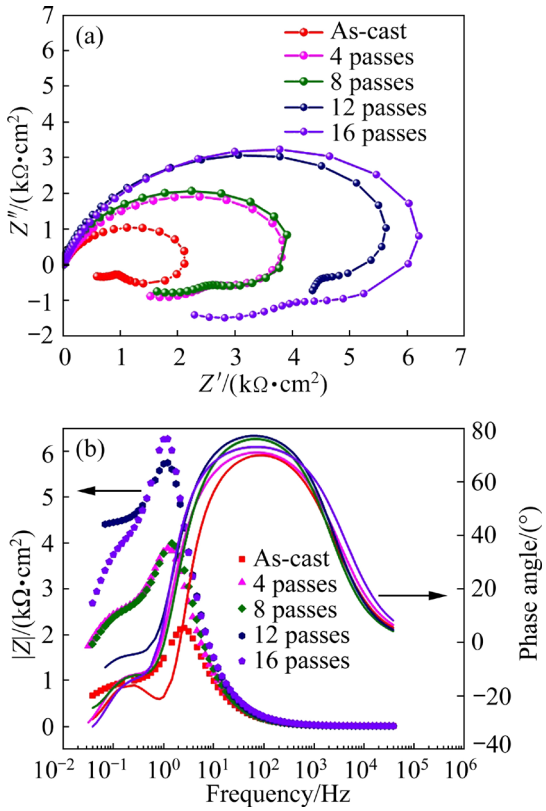

Fig. 12 EIS data of Al−5Zn alloys after different ECAP passes in 3.5 wt.% NaCl solution: (a) Nyquist plots; (b) Bode plots

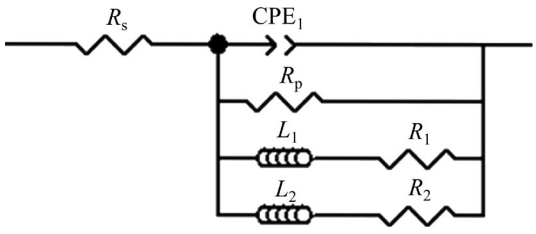

Fig. 13 Equivalent circuit and its possible corresponding physical structure of Al−5Zn alloy in 3.5 wt.% NaCl solution

Generally, the CPE_1 value corresponds to a thicker passivation film. As shown in Table 3, CPE_1 first decreases with increasing ECAP passes, reaching a minimum after 12 passes, and subsequently increases. This trend indicates that the passivation film thickness increases up to 12 passes and then decreases.

Table 3 Parameters of equivalent circuit of Al−5Zn alloys after different ECAP passes

Sample	R_s/ ($\Omega\cdot cm^2$)	CPE_1/ ($\mu F\cdot cm^2$)	n	R_p/ ($\Omega\cdot cm^2$)	L_1/ ($H\cdot cm^2$)	R_1/ ($\Omega\cdot cm^2$)	L_2/ ($H\cdot cm^2$)	R_2/ ($\Omega\cdot cm^2$)
As-cast	9.85	27.94	0.8466	3038	289.2	1467	4894	5096
4 passes	9.92	24.95	0.8402	5527	15370	1215	1337	498.1
8 passes	10.47	18.31	0.9003	5251	1221	5167	1410	1858
12 passes	10.60	15.30	0.9039	7841	666.1	0	2317	1036
16 passes	9.17	19.02	0.8499	9706	18520	1825	2015	73950

n is the dispersion exponent of the constant phase element (CPE)

Figure 14 and Table 4 show the potentiodynamic polarization curves of the Al−5Zn alloys and the corrosion potential (φ_{corr}) and current density (J_{corr}) estimated via Tafel fitting, respectively. Among the studied samples, the as-cast sample exhibits the highest J_{corr} value. J_{corr} decreases gradually with the increase of the number of ECAP passes. After 4 and 8 passes, J_{corr} exhibits the same order of magnitude (3.99×10^{-6} and 2.80×10^{-6} A/cm^2, respectively). After 12 passes, J_{corr} significantly decreases to 5.382×10^{-7} A/cm^2. In addition, after 16 passes, J_{corr} slightly decreases to 4.065×10^{-7} A/cm^2.

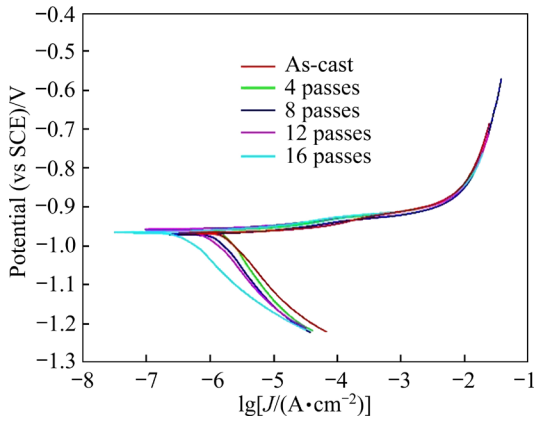

Fig. 14 Potentiodynamic polarization curves of Al−5Zn alloys after different ECAP passes in 3.5 wt.% NaCl solution

Table 4 Corrosion potential (φ_{corr}) and corrosion current density (J_{corr}) of Al−5Zn alloys after different ECAP passes

Sample	φ_{corr}(vs SCE)/V	J_{corr}/(A·cm^{-2})
As-cast	−0.964	7.43×10^{-6}
4 passes	−0.961	3.99×10^{-6}
8 passes	−0.970	2.80×10^{-6}
12 passes	−0.9688	5.382×10^{-7}
16 passes	−0.9663	4.065×10^{-7}

This indicates that ECAP has a significant effect on the corrosion rate of the Al−5Zn alloy in a 3.5 wt.% NaCl solution.

Figure 15 shows surface corrosion morphologies of Al−5Zn alloys obtained from electrochemical experiments. Significant intergranular corrosion is observed in the as-cast sample. Figure 15(a) shows some large corrosion pits on the surface and large-width corrosion cracks spreading along the grain boundaries. Figure 15(b) shows a significant reduction in the number and width of the surface corrosion cracks after 4 passes, resulting in a multitude of short corrosion lines. As the number of ECAP passes increases, the corrosion lines are transformed into numerous dotted lines; however, Figs. 15(c, d) show that the size and distribution of these dots (corrosion pits) are not uniform after 8 and 12 passes. After 16 passes, the corrosion pits are distributed more evenly, as shown in Fig. 15(e).

We conducted a 7 d immersion corrosion test to further observe the longitudinal corrosion progression. Figure 16 shows longitudinal-section OM images of the samples after different ECAP passes after the 7 d immersion. It is evident that the corrosion starts from the grain boundaries and spreads to the depth of the sample (as marked by the yellow rectangle shown in Fig. 16(a)). When all grain boundaries around a grain are corroded, the entire grain exfoliates (as marked by the blue rectangle shown in Fig. 16(a)), resulting in the largest corrosion pits (their typical depth and width are ~33 and ~86 μm, respectively) of the as-cast sample. In conjunction with Fig. 15(a), it is concluded that the corrosion of the as-cast sample is intergranular. After 4 ECAP passes, a single corrosion pit exhibits a pyramidal shape, where the deepest and widest points are ~20 and ~30 μm, respectively; these values are much smaller than those of the as-cast sample. However, as shown in

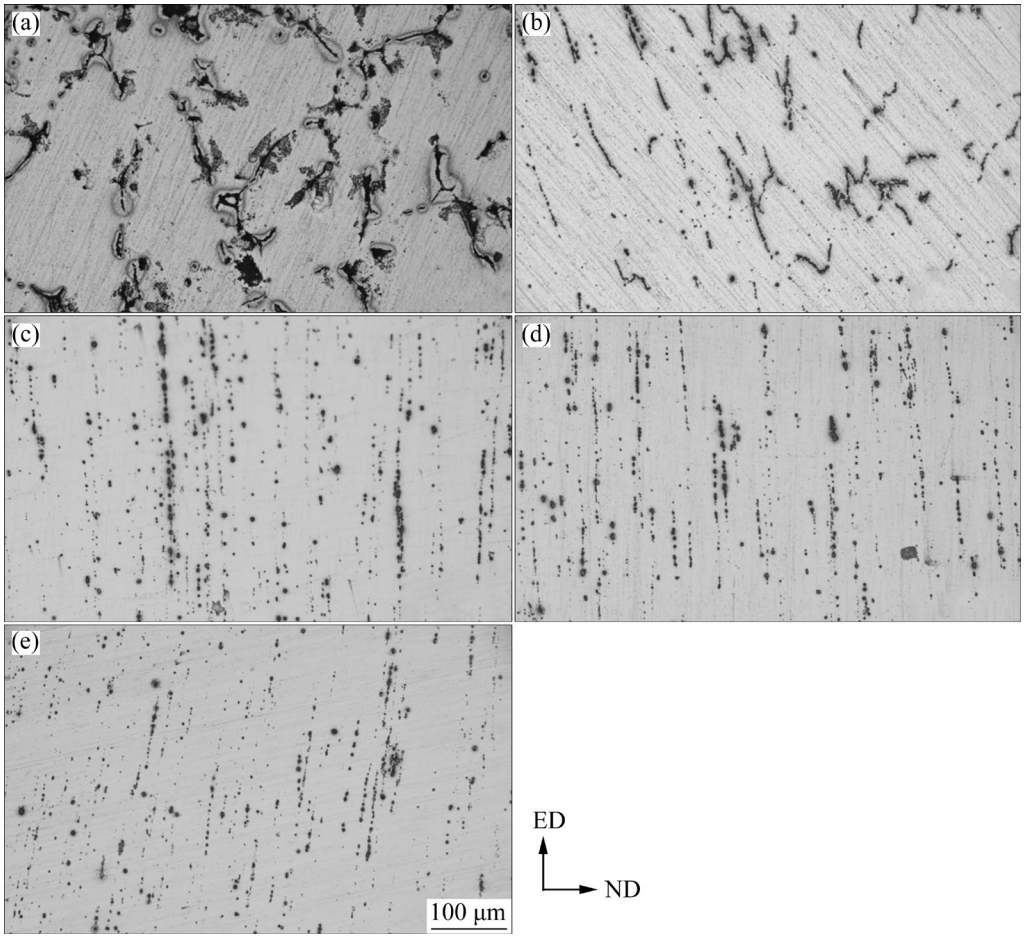

Fig. 15 Surface corrosion morphologies of Al−5Zn alloys after electrochemical experiments: (a) As-cast; (b) 4 passes; (c) 8 passes; (d) 12 passes; (e) 16 passes

Fig. 16(b), the pyramidal pits merge into large pits, which is consistent with the surface morphology indicated by the short corrosion lines (Fig. 15(b)). Consequently, after 4 passes, the sample exhibits pitting corrosion. As shown in Fig. 16(c), the depth and width of a single pit decrease, although the pits still merge (corresponding to the corrosion dotted lines on the surface shown in Fig. 15(c)) as the number of ECAP passes increases. Figure 16(d) shows that when the number of ECAP passes increases to 12, the majority of the corrosion pits are tiny and autonomous. After 16 passes, most of the corrosion pits are very small and independent of each other (as marked by the yellow rectangle shown in Fig. 16(e)), indicating that the corrosion rate significantly decreases.

4 Discussion

The experimental results demonstrate that ECAP can significantly improve the corrosion resistance of the Al−5Zn alloy. Its grain size, secondary-phase characteristics, and dislocations change significantly after ECAP. In this study, we attempted to distinguish the effects of these three factors on the corrosion behavior of the Al−5Zn alloy.

Regarding grain size, it has been reported that high-density grain boundaries can quickly enrich the passivation elements and form a dense passivation film on the material surface [27,28]. Compared with the as-cast sample, the grain size of the ECAPed samples decreases significantly (from 30 to ~3 μm, as shown in Fig. 5). We expect the ECAPed samples to exhibit improved corrosion resistance. Additionally, as the number of ECAP passes increases, the grain size does not change significantly. Therefore, we infer that the grain size is not the dominant factor in improving the corrosion resistance of the ECAPed samples.

The characteristics of the precipitates (including size and distribution) are an important

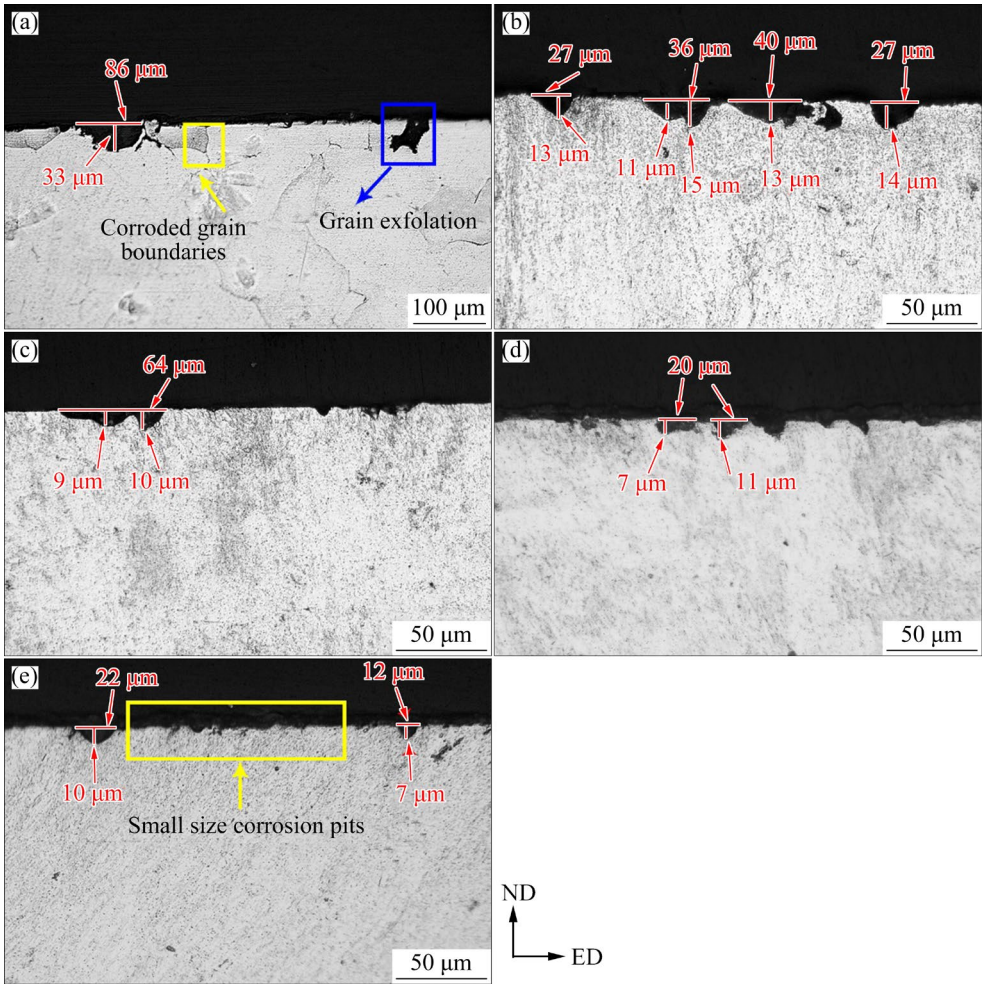

Fig. 16 OM images of longitudinal-section of ECAPed Al−5Zn alloys after 7 d immersion corrosion experiment: (a) As-cast; (b) 4 passes; (c) 8 passes; (d) 12 passes; (e) 16 passes

factor affecting the corrosion resistance of the Al−5Zn alloy. Figures 2(a, b) show that many coarse Zn phases are distributed along the grain boundaries in the as-cast sample. These phases gradually break and disperse more evenly as the number of ECAP passes increases. The potential of the Zn phases (−0.76 V) in the Al−Zn alloy is less negative than that in the Al matrix (−1.66 V). The Zn phase is less susceptible to corrosion due to its less negative potential. Therefore, after the corrosion of the Al matrix, which surrounds the Zn phase, the abscission of the Zn phases from the matrix typically leads to the formation of corrosion pits. The fragmentation of the Zn phase effectively reduces the size of the corrosion pit. In other words, a large anode−small cathode microcell is formed by the Al matrix (with a more negative potential) and the Zn phase (with a less negative potential). Decreasing the size of the Zn phase further reduces the cathode-to-anode area ratio, thereby weakening the degree of galvanic corrosion [29].

In addition, after 16 passes, the dislocation density distribution in the Al−Zn alloy becomes more uniform. This is attributed to the increased recrystallization rate of the alloy after 16 passes, as shown in Fig. 6(d). The ECAP process causes the annihilation and reorganization of the dislocations within the alloy during dynamic recrystallization, especially in regions with high dislocation density [30]. Therefore, after 16 passes, regions with high dislocation density undergo significant dynamic recrystallization, whereas regions with low dislocation density are less affected, ultimately leading to a uniform dislocation density distribution. Figures 3(f, g) and 5(c, d) show that after 16 passes, the sizes of the Zn phase and grains remain almost unchanged compared with those of 12 passes; however, the corrosion resistance is marginally

superior. This can be attributed to the uniform distribution of dislocations in Al−5Zn alloy, which reduces the promotion effect of dislocations on the development of pitting corrosion near the Zn phase [31]. Therefore, the uniform distribution of dislocations is another important factor that improves the corrosion resistance.

The above analysis indicates a potential corrosion mechanism for the Al−5Zn alloy in a 3.5 wt.% NaCl solution, as shown in Fig. 17. The Al_2O_3 passivation film must be initially formed on the Al matrix before gradually spreading to the Zn phase surface because it cannot be formed directly on the Zn phase [32]. Consequently, the passivation layer on the Zn phase is thinner than that on the Al matrix. Additionally, the size of the Zn phase significantly affects the uniformity of the passivation film. Compared with that in the as-cast sample, the Zn phase in the alloy after ECAP is smaller and requires less time for the passivation film to completely cover it. Therefore, as shown in Figs. 17(a, c), there is sufficient time for the passivation film on the Zn phase to thicken, thus increasing the erosion resistance to Cl^-.

The second stage of the corrosion is reached when the passivation film near the Zn phase is corroded, as shown in Figs. 17(b, d). The morphological characteristics of the Zn phase and the presence of nanoscale Zn in the crystal significantly affect the corrosion rate. The Zn phase in the as-cast alloy is large and continuously distributed along the grain boundary, whereas the Zn phase in the ECAPed alloy exhibits a small size and is evenly distributed. The Zn phase falls off the Al matrix when the matrix that surrounds it undergoes total corrosion caused by microgalvanic corrosion. The large Zn phase causes a large pit on the substrate surface, facilitating the growth of the corrosion. The small Zn phase causes a small corrosion pit after the corrosion process. This means fewer Cl^- ions in the corrosion pit, which slowly migrate from the solution to the pit and stop the corrosion pit from growing. However, after 12 passes, some nanoscale Zn phases appear inside the grains, balancing the potential between the Al matrix and the Zn phase to a certain extent and reducing the corrosion rate of the Al matrix.

Figure 17(e) shows the evolution of the corrosion pit in relation to the dislocations and nanoscale Zn phases. When there is no Zn phase near the corrosion pit, the number of dislocations determines its development rate. The TEM images show that some grains contain a large number of dislocations (Fig. 10). As a high-energy structure, dislocations tend to accumulate Cl^-, leading to a fast corrosion rate in grains with high dislocation density. When the nanoscale Zn phases are present at the edge of the corrosion pit, a process similar to the second stage corrosion occurs; the nanoscale Zn phases detach and leave new small corrosion pits. The process continues until it encounters a new micron-sized Zn phase.

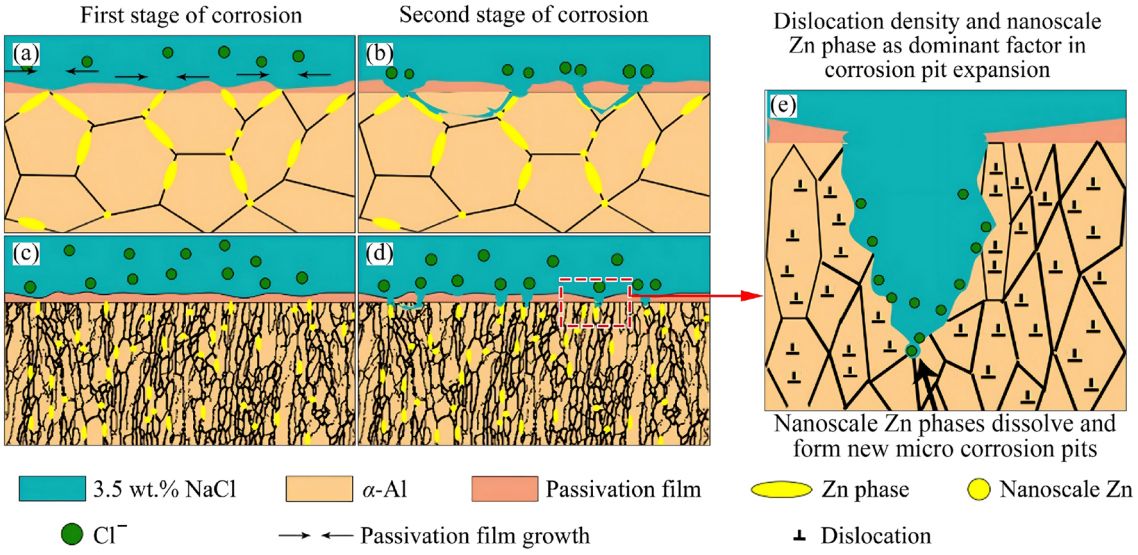

Fig. 17 Schematic diagrams depicting corrosion mechanism of Al−5Zn alloy in 3.5 wt.% NaCl solution: (a, c) First stage of corrosion in as-cast and ECAPed alloys, respectively; (c, d) Second stage of corrosion in as-cast and ECAPed alloys, respectively; (e) Pitting evolution related to dislocations and nanoscale Zn phase

5 Conclusions

(1) The size of the Zn phase and the dislocation density of the Al−5Zn alloy can be controlled by the number of ECAP passes. Compared with the untreated sample, the Zn phase in the treated sample is severely fractured after several ECAP passes and is reduced to a minimum of 2 μm; no further reduction is observed after 12 passes; the most uniform dislocation in the alloy is observed after 16 passes.

(2) The EIS results show that after 16 passes, the Al−5Zn alloy exhibits its highest R_p value (9706 Ω·cm^2) and its lowest corrosion current density (4.065×10^{-7} A/cm^2) as well as excellent comprehensive mechanical properties (UTS, YS, and EL were 224 MPa, 199 MPa, and 21.3%, respectively).

(3) The corrosion type of the Al−5Zn alloy changes from intergranular corrosion in the as-cast sample to pitting corrosion in the ECAPed samples. By increasing the number of ECAP passes to 8, the corrosion depth decreases significantly. By further increasing the number of passes, the corrosion depth remains relatively unchanged, but the average corrosion width significantly decreases.

(4) The main reasons for the excellent corrosion resistance of the Al−5Zn alloy after 16 passes are the fragmentation and uniform distribution of the Zn phase and the evenly distributed dislocations. The fine Zn phase causes a size reduction in the corrosion pits and a significant weakening of the large anode−small cathode effect. Additionally, the uniformly distributed dislocations cause a reduction in the growth rate of corrosion pits.

CRediT authorship contribution statement

Yu-na WU: Conceptualization, Methodology, Writing − Review & editing, Funding acquisition; **Chong-guang YUE:** Data curation, Writing − Original draft; **Ting YUAN**: Conceptualization, Methodology; **Lin WANG:** Methodology, Funding acquisition; **Dan SONG**: Conceptualization, Methodology; **Huan LIU:** Conceptualization, Writing − Review & editing, Funding acquisition; **Jing-hua JIANG:** Methodology, Supervision; **Jing BAI:** Conceptualization, Methodology, Funding acquisition; **Ai-bin MA:** Conceptualization, Supervision.

Declaration of competing interest

The authors declare that they have no known competing financial interests or personal relationships that could have appeared to influence the work reported in this paper.

Acknowledgments

The authors would like to acknowledge the financial support from the National Natural Science Foundation of China (No. 52303390), the Natural Science Foundation of Jiangsu Province, China (No. BK20230963), the Jiangsu Provincial Key Research and Development Program, China (No. BE2021027), the Nanjing Major Science and Technology Project, China (No. 202309015), the Opening Project of Jiangsu Key Laboratory of Advanced Structural Materials and Application Technology, China (No. ASMA202305), and the Suzhou Science and Technology Project, China (Nos. SJC2023005, SZS2023023).

Data availability

The data that support the findings of this study are available on request from the corresponding author.

References

[1] GUAN Ren-guo, TIE Di. A review on grain refinement of aluminum alloys: Progresses, challenges and prospects [J]. Acta Metallurgica Sinica (English Letters), 2017, 30: 409−432.

[2] GAIROLA S, JAYAGANTHAN R. Influence of heat treatment, microstructure evolution, and damage mechanism on high cycle fatigue behaviour of additively manufactured Ti-modified Al 2024 alloy [J]. Materials Characterization, 2023, 203: 113047.

[3] KE Bin, YE Ling-ying, ZHANG Yong, TANG Jian-guo, LIU Sheng-dan, LIU Xiao-dong, DONG Yu, WANG Ping. Enhanced mechanical properties and corrosion resistance of an Al−Zn−Mg aluminum alloy through variable-rate non-isothermal aging [J]. Journal of Alloys and Compounds, 2022, 890: 161933.

[4] CHUVIL′DEEV V N, NOKHRIN A V, KOPYLOV V I, GRYAZNOV M Y, SHOTIN S V, LIKHNITSKII C V, KOZLOVA N A, SHADRINA Y S, BERENDEEV N N, MELEKHIN N V, NAGICHEVA G S, SMETANINA K E, TABACHKOVA N Y. Investigation of mechanical properties and corrosion resistance of fine-grained aluminum alloys Al−Zn with reduced zinc content [J]. Journal of Alloys and Compounds, 2022, 891: 162110.

[5] MA Yu-kun, WANG Ming-xing, LIU Ya-nan, CAI Bin. Microstructures and corrosion behaviors of Al−6.5Si−0.45Mg−*x*Sc casting alloy [J]. Transactions of Nonferrous Metals Society of China, 2022, 32: 424−435.

[6] ZHAO Pei-hao, WU Xiao-lan, GAO Kun-yuan, WEN Sheng-ping, RONG Li, HUANG Hui, WEI Wu, NIE Zuo-ren. Effect of Zn/Mg ratio on microstructure and mechanical properties of Al−Zn−Mg alloys [J]. Materials Letters, 2022, 312: 131676.

[7] TAN Pan, QIN Jin, QUAN Xiang, YI Dan-qing, WANG Bin. Co-strengthening of the multi-phase precipitation in high-strength and toughness cast Al−Cu−Zn−Mg alloy via changing Zn/Mg ratios [J]. Materials Science and Engineering: A, 2023, 873: 145024.

[8] PÉREZ C J L, IRIGOYEN R L, ARBIZU I P, PÉREZ D S, IRIARTE J L, JUAN P B F. Analysis of tribological properties in disks of AA-5754 and AA-5083 aluminium alloys previously processed by equal channel angular pressing and isothermally forged [J]. Metals, 2020, 10: 938.

[9] AFIFI M A, WANG Ying-chun, PEREIRA P H R, WANG Yang-wei, LI Shu-kui, HUANG Yi, LANGDON T G. Characterization of precipitates in an Al−Zn−Mg alloy processed by ECAP and subsequent annealing [J]. Materials Science and Engineering: A, 2018, 712: 146−156.

[10] TANG Lei, PENG Xiao-yan, JIANG Fu-qing, LI Yao, XU Guo-fu. Strong and ductile Al−Zn−Mg−Zr alloy obtained by equal angular pressing and subsequent aging [J]. Transactions of Nonferrous Metals Society of China, 2022, 32: 1428−1441.

[11] YUE Chong-guang, LI Yun, WU Yu-na, LIU Huan, JIANG Jing-hua, MA Ai-bin. An overview of the effect of severe plastic deformation on corrosion resistance of aluminum alloys used in transportation [J]. Modern Transportation and Metallurgical Materials, 2023, 3: 82−88. (in Chinese)

[12] QIN Jin, LI Zhi, MA Ming-yang, YI Dan-qing, WANG Bin. Diversity of intergranular corrosion and stress corrosion cracking for 5083 Al alloy with different grain sizes [J]. Transactions of Nonferrous Metals Society of China, 2022, 32: 765−777.

[13] SEIKH A H, BAIG M, REHMAN A U. Effect of severe plastic deformation, through equal-channel angular press processing, on the electrochemical behavior of Al5083 alloy [J]. Applied Sciences, 2020, 10: 7776.

[14] XIONG Han-qing, ZHOU Yue-xin, YANG Peng, KONG Char-lie, YU Hai-liang. Effects of cryorolling, room temperature rolling and aging treatment on mechanical and corrosion properties of 7050 aluminum alloy [J]. Materials Science and Engineering: A, 2022, 853: 143764.

[15] IKEUBA A I, ZHANG B. Electrochemical investigation of the anodic hydrogen evolution on $MgZn_2$, Mg_2Si, and $Al_4Cu_2Mg_8Si_7$ intermetallic phases [J]. Journal of Solid State Electrochemistry, 2023, 27: 111−123.

[16] CHEN Yu-meng, WU Yu-na, GENG Jun, LIU Huan, SONG Dan, JIANG Jing-hua, FANG Feng, MA Ai-bin. Pre-precipitating promoted by microshear bands effectively circumvents strength-ductility trade-off of RT-rolled Al−6Zn−1Mg alloy [J]. Journal of Materials Research and Technology, 2024, 28: 2767−2777.

[17] LIU Huan, HUANG He, ZHANG Yue, XU Yan, WANG Ce, SUN Jia-peng, JIANG Jing-hua, MA Ai-bin, XUE Feng, BAI Jing. Evolution of Mg−Zn second phases during ECAP at different processing temperatures and its impact on mechanical properties of Zn−1.6Mg (wt.%) alloys [J]. Journal of Alloys and Compounds, 2019, 811: 151987.

[18] LI Gui-sheng, PAN Xin-yuan, JIANG Jin, LI Jing-hui, XIE Ling-ling, LIU Hai-tao, ZHANG Ming-ya. Achieving ultra-fine grains and high corrosion resistance of Al−Zn−Mg−Cu alloy by ECAP and post cold rolling [J]. Journal of Materials Research and Technology, 2023, 26: 7354−7368.

[19] SONG Dan, MA Ai-bin, JIANG Jing-hua, LIN Pin-hua, YANG Dong-hui. Corrosion behavior of ultra-fine grained industrial pure Al fabricated by ECAP [J]. Transactions of Nonferrous Metals Society of China, 2009, 19: 1065−1070.

[20] CABIBBO M, SANTECCHIA E, MENGUCCI P, BELLEZZE T, VICERÉ A. The role of cryogenic dipping prior to ECAP in the microstructure, secondary-phase precipitation, mechanical properties and corrosion resistance of AA6012 (Al−Mg−Si−Pb) [J]. Materials Science and Engineering: A, 2018, 716: 107−119.

[21] QUARTIERMEISTER M V, MAGALHÃES D C C, VACCHI G S, BRAGA D P, SILVA R, KLIAUGA A M, SORDI V L, ROVERE C A D. On the pitting corrosion behavior of ultrafine-grained aluminum processed by ECAP: A statistical analysis [J]. Materials and Corrosion, 2020, 71: 1244−1256.

[22] HE Shu-heng, WANG Ce, SUN Chao, ZHANG Yue, YAN Kai, JIANG Jing-hua, BAI Jing, XUE Feng, LIU Huan. Corrosion properties of ECAP-processed Mg−Al−Ca−Mn alloys with separate Al_2Ca and Mg_2Ca phases [J]. Transactions of Nonferrous Metals Society of China, 2020, 32: 2527−2540.

[23] JI Yuan-yuan, XU Yun-ze, ZHANG Bin-bin, BEHNAMIAN Y, XIA Da-hai, HU Wen-bin. Review of micro-scale and atomic-scale corrosion mechanisms of second phases in aluminum alloys [J]. Transactions of Nonferrous Metals Society of China, 2021, 31: 3205−3227.

[24] LU Hong-jian, XU Wei-feng, WANG Huan, WANG Xian-zong. Microstructure evolution and its effect on the corrosion of dissimilar aluminum alloys friction stir welding joint [J]. Corrosion Science, 2023, 220: 111249.

[25] WU Yu-na, LIAO Heng-cheng, TANG Yun-yi. Enhanced high-cycle fatigue strength of Al−12Si−4Cu−1.2Mn−T6 cast aluminum alloy at room temperature and 350 °C [J]. Materials Science & Engineering: A, 2021, 825: 141817.

[26] CHEN Yu-meng, WU Yu-na, LI Yun, PENG Zhi-yang, LIU Huan, MA Ai-bin, JIANG Jing-hua, YUAN Ting. RT ECAP and rolling bestow high strength and good ductility on a low lithium aluminum alloy [J]. Journal of Materials Research and Technology, 2023, 25: 5561−5574.

[27] MARTA O, EWA U, LECH O, MAŁGORZATA L. The effect of grain size and grain boundary misorientation on the corrosion resistance of commercially pure aluminium [J]. Corrosion Science, 2019, 148: 57−70.

[28] ROCHET C, VERON M, RAUCH E F, LOWE T C, ARFAEI B, LAURINO A, HAROUARD J P, BLANC C. Influence of equal-channel angular pressing on the microstructure and corrosion behaviour of a 6xxx aluminium alloy for automotive conductors [J]. Corrosion Science, 2020, 166: 108453−108453.

[29] LIU Qu, CHEN Gao-qiang, ZENG Shen-bo, ZHANG Shu-ai. Effect of microstructure refinement on the corrosion of AZ91D magnesium alloys [J]. Journal of Tsinghua University, 2019, 59: 765−771. (in Chinese)

[30] HUANG K, LOGÉ R E. A review of dynamic recrystallization

phenomena in metallic materials [J]. Materials & Design, 2016, 111: 548−574.

[31] HAIDER K S, SANGEUN P, KWANGJUN E, BOK S J, GI K J, HYOKYUNG S. Dislocation-aided electrochemical behavior of precipitates in stress corrosion cracking of Al−Zn−Mg−Cu alloys [J]. Materials Characterization, 2022, 190: 112019.

[32] SON I J, NAKANO H, OUE S, KOBAYASHI S, FUKUSHIMA H, HORITA Z. Pitting corrosion resistance of anodized aluminum-copper alloy processed by severe plastic deformation [J]. Materials Transactions, 2008, 49: 2648−2655.

通过调节 Zn 相和位错分布显著提高 Al−5Zn 合金的耐蚀性

吴玉娜[1,2]，岳崇光[1,2]，袁 婷[3]，王 琳[1]，宋 丹[1]，刘 欢[1]，江静华[1]，白 晶[4]，马爱斌[1]

1. 河海大学 材料科学与工程学院，常州 213200；
2. 河海大学 宿迁研究院，宿迁 223800；
3. 常熟理工学院 化学与材料工程学院，常熟 215500；
4. 东南大学 材料科学与工程学院，南京 211189

摘 要：由于第二相种类的多样性，7xxx 系铝合金强度和耐蚀性的平衡很难实现。本文作者选用 Al−5Zn 二元合金作为 7xxx 系铝合金的简化代表，并采用 4 种不同的等通道转角挤压道次(4、8、12 和 16 道次)来调节合金中的 Zn 相和位错分布。通过电化学和拉伸试验测试，结合光学显微镜、扫描电子显微镜和透射电子显微镜等手段，研究了合金的腐蚀行为和力学性能。结果表明，经 16 道次 ECAP 后，Al−5Zn 合金具有最大的极化电阻和最低的腐蚀电流密度，同时具有良好的综合力学性能，其极限抗拉强度、屈服强度和伸长率分别为 224 MPa、199 MPa 和 21.3%。这种良好的耐蚀性和力学性能的结合主要归因于 Zn 相的破碎和均匀分布以及位错的均匀分布。

关键词：Al−Zn 合金；耐蚀性；Zn 相；位错；力学性能

(Edited by Wei-ping CHEN)